Paper III

Vertical mixing in the MIZ of the northern Barents Sea – results from numerical model experiments

Arild Sundfjord[1,2], Ingrid Ellingsen[3], Dag Slagstad[3] and Harald Svendsen[1]

[1] Geophysical Institute, University of Bergen, Bergen,

[2] Norwegian Polar Institute, Tromsø

[3] SINTEF Fisheries and Aquaculture, Trondheim

Accepted for publication in Deep-Sea Research-II.

Abstract

Numerical ocean model simulations of the marginal ice zone (MIZ) of the Barents Sea have been made for the years 2003-2005. As part of the CABANERA project, the model simulations provide a pre-history and context for interpretation of physical as well biological and chemical field data collected during the annual project cruises carried out in the Barents Sea MIZ in this period. Large-scale features as well as the temporal evolution of stratification and vertical mixing, from well-mixed winter conditions to the end of the ice-free season, are described. Modelled ice cover at the times of the annual project cruises is in agreement with that inferred from satellite data. Year-to-year differences in exchange of ice with the adjacent seas are found to be as important for changes in the overall heat budget of the Barents Sea as the variation in the inflow of warm Atlantic Water. A description is given of the simulated seasonal development of mixing and stratification in the MIZ, from winter via the melting period and through the productive summer season. Turbulent mixing forced by tidal currents and wind episodes is examined, and resulting hydrographical conditions and diffusivities are compared with previously published measurements of turbulence from the project cruises. Although the vertical and temporal extent to which such variable mixing influences the water column are realistically modelled, the strength of mixing may be inaccurately distributed. Most importantly, differences in modelled and observed water column stratification are identified. Near the surface, enhanced mixing appears to protrude too deeply in the model, and below the pycnocline the water column is excessively homogenized. Experiments with the Mellor-Yamada Level 2.5 turbulence scheme are compared with those from the Richardson-number scheme routinely used in the model, as well as simulations with increased vertical resolution and reduced horizontal grid cell size. Some important differences between

the two schemes are identified, but the Mellor-Yamada simulations are not found to yield significantly more realistic results. Increasing the vertical resolution only marginally improves the stratification profiles while simulations with horizontal grid resolution increased from 4×4 km^2 km to 800×800 m^2 allows for processes inducing significantly more energetic frontal mixing at the MIZ edge to be resolved.

Keywords

Modelling, vertical mixing, diffusivity, Barents Sea, marginal ice zone

1 Introduction

This work is part of CABANERA, a project studying the biogeochemical carbon cycle in the marginal ice zone (MIZ) of the Barents Sea. An important component of the CABANERA project has been the annual ship-based surveys in the Barents Sea MIZ in 2003-2005, covering lower-trophic-level biology, carbon chemistry and physics. Results from field studies are used as input for a coupled physical-biological model, specifically designed for this region, in which the different processes are integrated and the flow of organic and inorganic carbon can be simulated under differing environmental conditions (Wassmann et al., 2006). Other aspects of the project are more thoroughly described elsewhere in this volume (Wassmann, this issue).

Highly productive blooms in primary production are known to occur in the MIZs as the ice recedes in summer, providing pulses of food for higher trophic levels, both pelagic and benthic (Wassmann et al., 1996). Large amounts of dissolved inorganic carbon are then utilized in photosynthesis, and during the bloom and following ice-free period the shelf can act as a biological pump for atmospheric CO_2 (Bates, 2006). The intense blooms are strongly linked to the development of mixing conditions and stratification due to melting in the MIZ (Strass and Nöthig, 1996). The vertical mixing processes in the MIZ are poorly known. Sampling is difficult due to the ice conditions and data on turbulence from these regions are therefore scarce. Furthermore, knowledge about turbulent mixing from other areas may not be directly applicable in the MIZ environment due to the effects of ice on air-sea momentum exchange, and the large buoyancy fluxes associated with input of melt water or brine expulsion during freezing. During the CABANERA project turbulence measurements have been made in concert with collection of biological and chemical data. This provides a unique

opportunity to evaluate several aspects of the coupled physio-bio-chemical model used in the project (Wassmann et al., 2006), from the parameterizations of the smallest physical scales to the integrated effect these have on large-scale productivity. Reliable numerical modelling of biological processes on shallow shelves has been shown to depend on adequate representation of vertical mixing resulting from interaction between stratification and current shear from tides and wind-driven currents (see e.g. Jin et al., 2006).

The Barents Sea is dominated by two main water masses, warm and saline Atlantic Water (AW) primarily entering through the western boundary, and cold and less saline Arctic Water (ArW), formed locally as well as flowing in from the north and east (Pfirman et al., 1994). These two water masses are separated by the Polar Front and the areas south and north of this are often referred to as the Atlantic and Arctic domains, respectively. AW and ArW are substantially mixed and modified within the Barents Sea. AW, for instance, looses heat and salt and sinks below the ArW as it flows north-east, and eventually contributes to the Arctic Ocean halocline and intermediate waters (Rudels et al., 2004). The Barents Sea can therefore be described as a throughflow shelf, different from the other Eurasian Arctic shelves. For a more complete description of water masses, current systems, and the local modification processes, see e.g. Loeng (1991) and Pfirman et al. (1994).

Previous model studies have explored the general ocean circulation in the Barents Sea and connections between regional climatic forcing and local responses such as inflow of AW, changes in ice cover, and export of modified water masses to the adjacent areas (e.g. Ådlandsvik and Loeng, 1991; Budgell, 2005; Harms, 1992; Harms, 1997; Harms et al., 2005). Gjevik et al. (1994) simulated tides in the Barents Sea, with results in good agreement with available measurement time-series. More local phenomena have also been studied by means

of numerical models. Several papers focus on the Spitsbergenbanken area, investigating tidal currents (Kowalik and Proshutinsky, 1995), the Atlantic Water retrograde slope jet current (Li and McClimans, 1998) and more general circulation pattern and hydrography (Ådlandsvik and Hansen, 1998). The dynamics of the Polar Front in relation to AW inflow and topography were studied by Gawarkiewicz and Plueddemann (1995). The roles of wind and heat flux in determining ice and brine production in the Storfjorden polynya were assessed by Skogseth et al. (2004).

The ocean model used in the CABANERA project, referred to as SINMOD, has been used for studying different aspects of Barents Sea dynamics and biology for a number of years, e.g. general circulation (Slagstad and McClimans, 2005; Slagstad et al., 1990), large-scale ice dynamics and mixing (Støle-Hansen and Slagstad, 1991), and lower-trophic-level biology (Wassmann et al., 2006). Other experiments have targeted e.g. shelf-slope dynamics along the coast of North Norway, important for the inflow dynamics to the Barents Sea (Skarðhamar and Svendsen, 2005).

General features of the hydrodynamical model and specifics on the two different vertical diffusion schemes applied in the simulations are presented in section 2. In section 3.1, large-scale interannual differences in ice cover and heat fluxes in the area are presented, and the changes in advective fluxes that produce these differences are identified. Knowledge of the hydrographical development on longer time scales than those observed during the cruises is useful for interpretation of data from the intensive field campaigns. We therefore give a presentation of changes in vertical mixing in the Barents Sea as simulated by SINMOD, in the period before and during the productive season (section 3.2). A closer look at some examples of the effects of wind episodes and strong tides is provided in section 3.3. Measurements of

microstructure shear and hydrography were performed during the last two CABANERA cruises. These turbulence measurements have been reported in two papers, focussing on the energetics of the surface mixed layer (Fer and Sundfjord, 2006) and mixing in and below the pycnocline (Sundfjord et al., 2006). This data set provides a unique opportunity for comparing vertical mixing data from model simulations with *in situ* observations (section 3.4). Throughout section 3 we refer to ice drift stations made during the CABANERA cruises in 2004-2005. The stations are identified with roman numerals, and more thorough descriptions of them can be found in Sundfjord et al. (2006). The effects of using a different numerical mixing scheme than that routinely used in SINMOD, and increased model resolution, are illustrated in section 3.5. Finally, the results are discussed and suggestions for further model experiments and development are given in section 4.

2 Numerical model

2.1 General model features and input data

2.1.1 Model description

A 3D hydrodynamical model, referred to as SINMOD, was applied for the simulations. The z-level model is based on the continuity equation for an incompressible fluid and the equation of motion (Navier-Stokes). The former implies that flow into a water volume is balanced by equal flow out of it while the latter states that the acceleration of a fluid is determined by the vector sum of the forces acting on it; pressure gradients, gravity, friction (at boundaries (wind, sea bed) and internally), and on the Coriolis force. The prognostic equations are solved by finite differencing in an Arakawa C-grid (Mesinger and Arakawa, 1976). Computational demands are reduced by mode-splitting of the fast barotropic mode and slower baroclinic mode (Berntsen et al., 1981). The model calculates horizontal diffusivity of momentum using

biharmonic friction while horizontal diffusion of scalars applies diffusion coefficients as in Smagorinsky (1963).

Ice dynamics are calculated according to the model of Hunke and Dukowicz (1997). Parameters resulting from ice freezing/melting and motion are ice thickness and cover in percent for each grid cell. The thickness of the surface cell, which may also include sea ice, is adjusted for the effect of atmospheric pressure and long waves. For equations and more detailed descriptions of the model see Slagstad et al.(1990), Støle-Hansen and Slagstad (1991) and Slagstad and McClimans (2005).

2.1.2 Model setup and forcing

The model setup used here consists of a 20×20 km^2 cell grid comprising the North Atlantic from ~50°N and the Arctic Ocean (Figure 1), with smaller, finer-resolution sub-domains nested into it. The number of vertical cells and thickness of the deepest cell in each grid point are determined from bathymetry data from IBCAO (http://www.ngdc.noaa.gov/mgg/bathymetry/arctic/arctic.html). The large scale model is initialized with climatological temperature and salinity from the NODC (Levitus) World Ocean Atlas 1998. At depth >1000 m the model is continuously relaxed towards climatology. A synthetic ice cover is initially defined. A spin up period of five years is needed to get reasonable distributions of ice and hydrography, before starting simulation of the three project years 2003-2005.

The model is forced by NCEP Reanalysis data provided by the NOAA-CIRES ESRL/PSD Climate Diagnostics branch, Boulder, Colorado, USA *(*http://www.cdc.noaa.gov/*)*. Tidal forcing (K_1, M_2, N_2, S_2) is taken from TPXO (Egbert et al., 1994; Egbert and Erofeeva, 2002)

and mean fluxes through the open boundaries are prescribed (see Ellingsen et al., this issue). Climatological run-off values for the largest continental rivers are included while no land-sea freshwater fluxes are used for the archipelagos around the Barents Sea.

[**Figure 1 (map of model domain)**]

Nested into the large scale model is a 4×4 km^2 model containing the Greenland Sea, Norwegian Sea, Barents Sea, and parts of the Kara Sea and Arctic Ocean (Figure 1). This, in turn, provides initial fields and boundary conditions for the smaller area covering the northern and central Barents Sea, in which experiments with different vertical mixing schemes and increased vertical resolution (all in a 4×4 km^2 grid) and with increased horizontal resolution (800×800 m^2) were made. The nesting is done with a flow relaxation scheme (Martinsen and Engedahl, 1987). The standard vertical resolution consists of 10, 6×5, 10, 2×25, 4×50, 2×100, 200, 300 and 6×500 m cells. Experiments with double vertical resolution (in the depth range relevant for the Barents Sea including the inner shelf slope, here taken as 700 m), have cells of 2×5, 12×2.5, 2×5 m etc. Note that all experiments in the smallest model domain used boundary conditions from the larger 4×4 km^2 simulations made with the Richardson number scheme and standard horizontal and vertical resolution.

2.2 Vertical mixing

2.2.3 RI-number scheme

The vertical turbulent mixing coefficient, K_v, is calculated as a function of the (gradient) Richardson number (Ri) and the state of the sea surface (wind-waves);

$$K_v = K_{vm}\left[\frac{\operatorname{atan}(G(R_{i0} - R_i))}{\pi} + 0.5\right] + k_w(W, z)$$

In the Ri-dependent part of the coefficient, K_{vm} is the maximum vertical diffusion (the asymptotic value of K_v as Ri approaches minus infinity), R_{i0} is the threshold value of the Ri number where the current changes from laminar to turbulent, and G is a shape parameter. Ri is given as $\mathrm{Ri} = \frac{g}{\rho}\frac{\partial \rho}{\partial z} \Big/ \left(\frac{\partial U}{\partial z}\right)^2$, where ∂U^2 is the sum of the squared difference in u and v velocity between two adjacent vertical cells, ρ is density and g is gravitational acceleration. Parameters used in the model are $K_{vm} = 3\times10^{-2}$ m^2 s^{-1}, $R_{i0} = 0.65$ and $G = 30$ m^{-1}. According to Price et al. (1986) the flow near the surface becomes turbulent if Ri is smaller than about 0.65.

The term $k_w(W,z)$ is a function describing the contribution to vertical turbulent diffusion from wind-waves (at depth z) as a function of wave height, H, and wave period, T, (Ichiye, 1967):

$$k_W = 0.028\frac{H^2}{T}e^{-0.8z/H} \qquad (2)$$

H and T are related to fetch length and the wind speed (W) at 10 m height by the empirical equation from the JONSWAP programme (Hasselmann et al., 1973), while the depth attenuation coefficient is determined by cell interface depth and wave height H. For example, given a fetch length >500 km, W=10 m s^{-1} will enhance diffusivity at 10 m depth by ~4×10^{-3} m^2 s^{-1}. When ice thickness in a given cell is >0.1 m, no wind-wave mixing is assumed to take place.

When the water column is unstable (i.e. due to cooling or brine release when ice freezes), the vertical diffusion coefficient is increased to allow for efficient vertical convection. This diffusivity increase depends on the thickness of the adjacent layers and ranges from O(10^{-2}) m^2 s^{-1} in the surface layer and > unity between the thick deep layers in the Barents Sea. At each time point, 20 % of the mixing coefficient from the preceding calculation is retained,

meaning that events of enhanced mixing are somewhat dampened and prolonged. The minimum mixing coefficient is set to 10^{-7} m^2 s^{-1}. In the following we refer to the Ri-number scheme described above simply as RI.

2.2.4 Mellor-Yamada

The widely used Mellor-Yamada Level 2.5 scheme (Mellor and Yamada, 1982), in the following referred to as MY, uses the budget of turbulent kinetic energy (TKE) and associated turbulent length scales to compute local vertical mixing coefficients. Like the Ri-based diffusivity parameter described above, the MY scheme also uses the vertical gradients of velocity and density to determine values for diffusivity of momentum and scalars, but does so prognostically by closing the energy budget for the water column using physical length scales determined by distance to the boundaries. This scheme both advects and diffuses the TKE driving the mixing, and in effect it also applies information on the energy history, thus diffusing the signals in time. We have used the scheme modified as suggested by Galperin et al. (1988) and with coefficients from Kantha and Clayson (1994), a version used in many general ocean circulation models at present. The eddy diffusion parameters are found as $K=qlS$, where q is the turbulent kinetic energy (found from solving the Reynolds stress equation), l is the turbulent macro scale (found from the equations for turbulent mass flux and density variance), and S is a stability function given by l^2, q^2, stratification and several empirically determined constants. The differential equations yielding q and l are of the same form as the advection-diffusion equations for temperature and salinity but using q^2 and q^2l as variables for which to solve. K thus varies with the size of eddies (l), forcing (q), stratification, and boundary proximity. Minimum diffusivity values were $K_H = 1\times10^{-7}$ (diffusion of scalars), $K_M = 5\times10^{-7}$ (diffusion of momentum), $K_Q = 1\times10^{-8}$ (diffusion of TKE).

2.2.5 Implicit/numerical mixing

Vertical movements in a level model produce artificial scalar fluxes trough the level boundaries, leading to apparent vertical mixing or numerical diffusion. This comes in addition to the diffusivity calculated explicitly with the RI and MY schemes. In SINMOD the scalar transport equation is modelled with a total variation diminishing scheme, designed to produce minimal numerical diffusion (Yang and Przekwas, 1992).

When we refer to the vertical mixing coefficient K or vertical diffusivity in the following, it means vertical diffusivity of scalars unless otherwise is explicitly stated (e.g. diffusivity of mass or momentum).

3 Model results and comparison with observations

3.1 Large-scale features 2003-2005

The extent and duration of ice cover in the northern Barents Sea was rather different between the three survey years (Figure 2). 2003 had the largest summer extent. At the time of the cruise that year (10-20 July) a large part of the study area was still ice covered, and at minimum extent (late August/early September) ice was still present in the northernmost part of the Barents Sea. In mid-July 2004 there was only little ice left in the Barents Sea, and the rest of this had disappeared by the first half of August. Large open water areas were also found north of the northern islands and extending across the shelf break. 2005 was similar to 2004, but with ice disappearing yet earlier in summer and with even larger ice free areas north and north-east. For comparison with the survey times in 2003 and 2004, there was only a small ice covered area in the north-western Barents Sea in mid-July 2005, considerably less than in 2004 and much less than 2003. The ice cover extent at the survey periods from the model simulations is similar to that derived from satellites (Figure 2) (Kaleschke et al., 2001),

with the most notable difference being a larger simulated ice covered area in the eastern Barents Sea at the time of the July 2003 cruise.

[Figure 2. Ice cover from satellite and model, 2003-2005]

Water volume, ice and heat transports into and out of the Barents Sea were calculated from simulations with the larger 4×4 km^2 grid to quantify year-to-year changes in the overall heat budget for the survey area. Simulation data from transects across the major in- and outflow pathways (see Figure 3) were stored for every 0.5 hours through the three survey years, 2003-2005. Water volume fluxes were calculated from mean current values of all cells in each transect for the duration of each year. Heat fluxes were found as the product of volume flux and the temperature in individual cells, referenced to a temperature of -0.1 °C (for comparison with results of Simonsen and Haugan (1996), see section 4), times the specific heat capacity of water. An outflow of 1 Sv at 0.9 °C was included for the area south of Novaya Zemlya (Simonsen and Haugan, 1996), as data from this area were not available from the model. Ice volume fluxes were similarly calculated using the thickness and concentration in each cell at each sample time. Heat flux with ice transport was found as the sum of latent heat of fusion for the flux volumes plus (regular) heat flux using an ice mean temperature of -10°C and reference temperature -0.1°C, and calculating both frozen (to -1.8°C) and liquid states with respective heat capacities. The use of mean ice temperature -10°C was again chosen to correspond with Simonsen and Haugan (1996). Monthly mean fluxes were calculated as well as annual means.

[**Figure 3 (map of Barents Sea, transects and stations)**]

Fluxes calculated from the model data show little difference in heat fluxes within the water column from 2003 to 2004 (67.0 vs 64.8 TW into the Barents Sea, respectively). Heat fluxes

associated with ice transport, however, changed substantially, with a net heat loss of -9.8 TW in 2003 decreasing to only -1.5 TW in 2004 (Table 1). This was due mostly to a reversal of the net flow direction between Spitsbergen and Franz Josef Land. In 2003 there was a net influx of ice equivalent to a heat loss of -5.7 TW through these straits, while in 2004 there was a net export of 1.7 TW. Also, the export between Spitsbergen and Bear Island increased by about 1 TW during that period. According to the model simulations the transport change is mostly a seasonal phenomenon; in winter and spring there was a net ice inflow in the north in all years, while during summer there was a large net ice export in 2004, different from 2003.

In 2005, the net heat loss from ice transports was similar to that in 2004 (-1.3 TW). There was now a small influx between Spitsbergen and Franz Josef Land (-0.3 TW) but this was compensated by smaller import between Franz Josef Land and Novaya Zemlya, and reduced outflow south of Spitsbergen. The overall heat budget still showed a similar trend from 2004-2005 as between 2003 and 2004, as the inflow of warm water, in particular between Norway and Bear Island, increased to a total of 70.4 TW. Net heat import (ice plus water fluxes) for the years 2003-2005 amounted to 57.2, 63.3 and 69.1 TW, year-to-year increases of ~10%.

Most of the straits connecting the Barents Sea to the adjacent basins had similar current patterns. Figure 4 shows volume flux, temperature and resulting heat flux through a cross-section between Nordaustlandet and Kvitøya (mean values for 2005). Along the deeper part of the western slope of the strait, warm Atlantic Water (AW) flows southwards and into the Barents Sea, while a colder outflow is found at mid-depth on the eastern side. Surface fluxes are more variable, but often follow the large, deeper currents.

[**Figure 4 (Cross-section plot of volume flux, temperature and heat flux)**]

There are also interannual changes in modelled air-sea heat fluxes in the Barents Sea. From 2003 to 2004 there is only a marginal increase in heat loss from the ocean to the atmosphere (0.1 TW). Given the net increase in advective heat flux this implies that a net loss of multi-year ice could ensue, and/or an increase in the mean water temperature. From 2004 to 2005 there was a large increase in the net heat loss to the atmosphere (13.4 TW), larger than the increased advective heat flux that year and implying a mean cooling. For the whole period 2003 to 2005 the difference between changes in advective inflow and surface heat loss is small (1.6 TW) and no significant overall effect on sea temperature or ice cover would be expected from differences in the overall heat budget alone.

3.2 Seasonal changes in stratification and vertical mixing

The interplay between stratification, forcing and vertical mixing varies through the year, resulting in large differences in diffusivity between winter and the ice-free season. During winter the water column in the ArW domain of the Barents Sea is only weakly stratified and little external forcing is required to produce efficient mixing. Figure 5a shows mean modelled diffusivity for April 2004, when all of the northern Barents Sea was ice covered except a small area in the south-western corner (less than one percent of the total area). Diffusivities are averaged over cells in the depth interval 25-40 m, which is below the influence of the largest wind-driven mixing at this time. In most of the area the mean diffusivity is $>10^{-3}$ m^2 s^{-1}, and in many places in excess of 10^{-2} m^2 s^{-1}. Diffusivities are lower in the very northern part and the deeper south-western region. This is due to greater melting rates in these areas; inflow of AW leads to freshwater release which in turn produces a stronger and shallower pycnocline (not shown). As ice melting progresses, the pycnocline will be strongest and shallowest in the interior parts, suppressing mixing there. Figure 5b shows mean diffusivity for August 2004, when the whole region had become ice free apart from a small area (~1 %)

south of Franz Josef Land. Values are from the same depth range as above; the typical pycnocline interval for the ice-free season. Diffusivities in the ArW-dominated areas are now considerably lower than in winter (typically ~1-10×10^{-5} m^2 s^{-1}). Inflow of higher-salinity near-surface water in the south-west allows for stratification there to be modest and diffusivities higher. In the northern part there are also areas of enhanced pycnocline diffusivities (>10^{-4} m^2 s^{-1}). However, this is associated with shallow banks with strong tidal currents, and not with AW influence. The same northern areas had strong mixing also in April, implying that here the forcing is more important than buoyancy fluxes (except along the southern perimeter of Nordaustlandet). Other, equally shallow areas in the north-west (around 400-550 km along the ordinate axis in Figure 5b – confer Figure 3) have weaker tidal currents and therefore low diffusivities - it is the current shear that is important, not shallow depth as such. Smaller areas with enhanced diffusivity are seen also south of the northern islands. Note also the trench between Nordaustlandet and Kvitøya, one of few places where diffusivities are low during both winter and summer. Diffusivities are generally elevated in the southern part of the ArW domain. This is due to the ice disappearing earlier here; wind-driven erosion and deepening of the pycnocline has been in effect longer.

For a closer look at some of the more prominent features of the melting period, simulation data from CABANERA ice drift station X (see Figure 3 for location) are used as an example. In winter there is only weak stratification and thus little resistance to vertical overturning (see January in Figure 6). Mixing driven by velocity shear between ice and water can thus reach deep, and elevated levels of diffusivity are seen throughout the water column (Figure 6). Although the ice cover dampens turbulent breaking of wind-driven waves in the model, this is compensated for by the lack of water column stability in winter. As winter progresses into spring the deep water masses become denser, in part due to advection, while the upper part of

the water column becomes more stratified due to a stronger salinity gradient. This is accompanied by changes in the mixing regime; the depth to which under-ice mixing reaches decreases while diffusivities in the bottom boundary layer increase. In June and July when melting and freshwater input is largest, the depth to which wind mixing reaches is at a minimum. An intermediate layer subject to less intense vertical mixing is found at depths 50-150 m.

[Figure 6 (Temporal evolution of ice cover, density and diffusivity at St X)]

Modelled diffusivity below the wind-influenced surface cells varies primarily with the fortnightly tidal spring-neap cycle (see the quasi-regular near-bottom enhancement, particularly from April to August, in Figure 6). When semi-diurnal and diurnal flood-ebb variations are filtered out (over 25 hours), spring tide diffusivity values within the pycnocline, K_{pyc}, (where the pycnocline is defined as the interface depth between the two cells with the largest density gradient ($d\rho/dz$)) are typically 10 times larger than neap values. At e.g. station X, where tidal currents are modest, mean K_{pyc} is ~$5x10^{-6}$ m^2 s^{-1} at neap tides and ~$5x10^{-5}$ m^2 s^{-1} at spring tides (both examples from late winter). Diffusivity variations resulting from the dominant semi-diurnal tide (M_2) are similar to the spring-neap difference, typically varying by an order of magnitude of the mean values. Diffusivities within the pycnocline decrease from winter until the peak of the melting period. At 5 of the 6 ice drift stations considered here the mean pycnocline diffusivity averaged over several spring-neap periods decreases by ~80 % from winter to the time of maximum melting. At station XIII, characterized by strong tidal mixing, the mean pycnocline diffusivity (averaged over spring-neap) remains >10^{-4} m^2 s^{-1} throughout the melting period, with a seasonal decrease of ~25 %. For most stations the diffusivity within the pycnocline continues to decrease as summer progresses, but not as drastically as between winter and the end of the melting period. As melt water is introduced in

spring a shallower seasonal pycnocline develops in the MIZ. At the peak of melting the mean pycnocline depth is 15-20 m, compared with >40 m during mid-winter. The seasonal pycnocline deepens further when all ice has disappeared, by 10-15 m for all survey stations. During autumn and early winter (not shown) the water column looses buoyancy through surface cooling and the vertical distribution of density and diffusivity again resembles that seen in January.

3.3 Effects of wind episodes and tides

Wind forced mixing of the surface layer is suppressed as buoyancy input from melting ice is at its largest during summer. Figure 7 shows wind speed, salinity and diffusivity in the upper 40 m during the last part of the ice covered period at station X. In mid-June, wind speed of ~10 m s^{-1} was still sufficient to enhance mixing more than tenfold down to 20 m depth, and the upper water column was partially homogenized. During the following period of weaker wind the stratification increased along with continuous input of melt water, and the next time winds reached 10 m s^{-1} (see 3 and 8 July) no significant erosion of the stratification resulted. When all ice had disappeared (2 August) the same wind speeds again produced deep mixing, increasing the mixed layer depth to >20 m. Horizontal advection of near-surface water may also contribute to the simultaneous SML deepening and increased near-surface mixing (see the abrupt disappearance of ice around 2-3 August in Figure 6).

[Figure 7 (wind speed, salinity and diffusivity during melting period at St X)]

On the shallower banks where tidal currents are stronger, high diffusivities persist throughout the melting period. In Figure 8 currents, density and diffusivity is shown for the melting phase at station XIII, just west of Kvitøya. Fortnightly spring tides give strong mixing at all depths. Note how the depth of maximum spring tide currents increases with time - the depth

distribution of shear changes accordingly (not shown). Only in the first week of August, when stratification is strongest and at neap tides, are diffusivities $<10^{-4}$ m^2 s^{-1} in an intermediate depth interval. Concurrently, strong winds force deep mixing from above, and by the middle of August the water column stability starts decreasing. After all ice is gone, the input of buoyancy to the surface layer from solar heating is not sufficient to withstand the combined mixing from tidal currents and wind.

[Figure 8 (currents, density and diffusivity during melting period at St XIII)]

3.4 Comparison with observed hydrography and turbulence

In the following, modelled hydrography and vertical diffusivity is compared with measurements at selected locations in the MIZ. These are examples, to evaluate whether the model is capable of producing realistic simulations of observed combinations of forcing and stratification in the MIZ. One would expect neither modelled hydrography nor mixing to match observations exactly at any given point in time, as there are differences in the exact ice and water mass distribution as well as e.g. the hind-cast wind used for simulations being different from that observed *in situ*. The model profiles presented below are from dates (within the same periods) selected to have appropriate forcing for comparison with the observations. The turbulence measurements are from the CABANERA cruises in July/August 2004 and May/June 2005, described in Sundfjord et al. (2006), and we compare with measured diffusivities of mass which can be different from diffusivity of scalars for non-homogeneous turbulence (see Sundfjord et al., 2006).

Profiles of measured density in the upper 60 m for three locations in the northern Barents Sea MIZ, from late July 2004, are shown in Figure 9. Also shown are modelled density profiles, along with profiles from preceding 14-day periods to illustrate how stratification develops as

the ice melts. Figure 9 also shows profiles of modelled vertical diffusivity. At station X the measured CTD profile shows no proper surface mixed layer (SML), but a seasonal pycnocline with melt water is present. The model captures this development, but with a stronger pycnocline extending deeper than the one observed. The measured density profile shows lower-density water below the pycnocline, suggesting that some surface water has been mixed down. The modelled diffusivity at this station is low, typically around or less than 10^{-5} m^2 s^{-1}, at all depths. This agrees well with mean values from turbulence measurements at the same location (Sundfjord et al., 2006, see their Figure 9 with average values from the duration (1-1.5 days) of ice drift stations), for conditions of weak wind and modest tides. At XI, where tidal currents were stronger and wind speed was ~10 m s^{-1} at the time of measurements, a SML was both developing in the model and seen in the observations. Diffusivities here were generally higher than at X at all depths, with a pronounced near-surface peak (~10^{-2} m^2 s^{-1}) due to wind, and high values (~10^{-4} m^2 s^{-1}) below the seasonal pycnocline, in the model as well as observations. Below the depth interval of maximum stratification the modelled density is lower than at the previous station, implying that some surface water is mixed down. Tides are stronger at this location and the time-mean mixing within and below the pycnocline is therefore larger than at X. Shallower station XIII was characterized by strong tidal currents and little wind forcing. Vertical mixing was intense throughout the water column. A local minimum associated with the base of the strongest density gradient was seen at 30-40 m both in model and measured profiles, but diffusivity remained >10^{-4} m^2 s^{-1} at all depths during this time. The resulting density profile, both modelled and observed, is smoother than at the two deeper stations nearby.

[Figure 9. Vertical profiles of density and diffusivity.]

The general hydrographic features are realistically represented in the model also at the other ice drift stations where turbulence measurements were made, with the vertical distribution of surface melt water, Arctic Water and AW resembling that observed (not shown). At station XIV, north of the shelf break, the model SML develops above a pycnocline that is stronger and more well-defined than that observed, and the AW found below the pycnocline is more vertically homogeneous in the model. The modelled vertical mixing is realistic for the wind response in the upper ~20 m, but too low below this depth due to the large pycnocline stability ($K < 10^{-5}$ m^2 s^{-1} at 50 m, while observations showed $K \sim 10^{-4}$ $m^2 s^{-1}$ to at least 60 m). The station north of the Polar Front in the central Barents Sea, XVI, was similar to XIV with melt water above an AW layer. The modelled wind response is realistic also at this station. The development of a proper SML and seasonal pycnocline occurs later in the season in the model than that observed, in part due to differences in ice distribution. The weak density gradient below the pycnocline is similar in the model and the observations. At the easternmost station, XVII, the model shows winter-like mixing conditions remaining until well into June – weak stratification allowed for strong mixing from wind and the modest tidal forcing at this location. In the model, spurious high-intensity mixing events are seen to occur well below the surface (30-50 m) before stratification increases. When a seasonal pycnocline and eventually SML developed, the modelled upper-column mixing protrudes to depths comparable to that observed. Measurements at the ice-free reference station XVIII, located in AW south of the Polar Front, where winds reached gale force (>20 m s^{-1}), showed enhanced mixing to >40 m depth, erasing any stratification to that depth. This is similar to the modelled wind response, to ~50 m. Both CTD profiles and model simulations show a small temperature and density gradient below this depth (the entire water column consists of AW at this station), but again with the modelled hydrography being less stratified than that observed.

3.5 Simulations with MY scheme and increased resolution

3.5.1 Mellor-Yamada scheme

Simulations for the same area and periods as presented previously have been performed also with the Mellor-Yamada Level 2.5 vertical mixing scheme (MY). Here, differences between simulations with this and the standard SINMOD RI-scheme are identified. Upper water column mixing is stronger with the MY setup during winter. During the ice covered period the (weak) pycnocline is deeper at all the survey stations presented previously, on average by ~15 m. Pycnocline diffusivities are also higher during the ice covered period, by a factor 1.2-4.7 at most survey locations. An exception to this is station XVII where large mean winter pycnocline diffusivity, due to the very low water column stability, is 90 times the corresponding value from RI simulations. As in the RI simulations, diffusivities decrease with the input of melt water in spring. The development of the melt-water layer is also similar for the two schemes, but with mean pycnocline depth ~5 m greater with MY. Ice disappears at similar times with the two schemes; the difference is not more than 5 days at any station, with ice disappearing earlier in the MY simulations when different.

Generally, the upper water column representation of hydrography in the melting season discussed in the previous sections is more closely reproduced by the standard RI scheme. Both schemes generally produce deeper SMLs and pycnoclines than those observed (see RI density profiles in Figure 9), MY more so than RI. Below the surface mixing layer and the pycnocline the MY setup mostly produces mixing around a "background level" of 10^{-5} m^2 s^{-1}. Enhanced mixing (above this "background level") occurs only between the near-bottom cells and at spring tides, and this rapidly decays away from the deepest cells. However, both schemes homogenize the sub-pycnocline water column too much. An example of the

differences is given in Figure 10. The figure shows mean diffusivity values for a neap and a spring tide period in a transect west of Kvitøya, covering both deep and shallow grid cells and different (mean) wind conditions, during the melting period. Currents from MY simulations (not shown) are similar to those shown for RI, but with slightly lower values except in the core of the mid-depth current maximum and near the surface on the eastern side. During the neap period the RI simulation has elevated near-bottom diffusivities over depths of at least 100 m. An intermediate layer with enhanced diffusivity is seen from 75-100 m, between the minimum diffusivities in the pycnocline (30-50 m depth) and below 100 m. The MY neap results show shallow enhancement only in the three easternmost cell columns and near the surface. There are no very low values associated with the pycnocline - the entire interior water column has $K \sim 10^{-5}$ m^2 s^{-1}. During spring tides the near-bottom enhancement effect is seen virtually throughout the transect in the RI data, again with the exception of the pycnocline over the deepest part where $K \sim 10^{-6}$ m^2 s^{-1}. The MY simulation now produced high deep diffusivities also in the deep part of the transect, even more so than RI. Note that winds were stronger during the neap period (mean 6.2 m s^{-1} compared with 3.7 m s^{-1} for the spring period), hence the higher and nearly uniform near-surface diffusivities during that time, particularly in the MY simulations.

[Figure 10. Transect from Kvitøya west showing mean current speeds and MY vs RI K for spring and neap periods.]

At shallow station XIII (just south of the transect presented above), enhanced mixing is seen at all depths during spring tides in the MY simulations (Figure 11). Mean MY diffusivity levels in the pycnocline during the melting period are nevertheless as low as $\sim 6 \times 10^{-5}$ m^2 s^{-1}. This is lower than that modelled with the RI setup where diffusivities were above the "background level" of 10^{-5} m^2 s^{-1} even at ebb tides.

[Figure 11. Time-plot of RI and MY mixing at XIII]

3.5.2 Double vertical resolution

RI simulations with twice the vertical resolution of the standard runs (see section 2.1.2) introduced some changes to the vertical distribution of mixing and hydrography. Upper-layer mixing was very similar; the development of melt water stratification and SMLs were almost identical. The pycnocline was often somewhat less steep/abrupt, i.e. closer to that observed. High near-bottom diffusivities were confined to a smaller depth interval but the resulting changes in deep stratification (compared with the standard resolution simulations) introduce different baroclinicity of the tidal currents, resulting in different shear patterns and over time reducing the difference in vertical distribution of mixing between the two model setups. Water properties below the pycnocline were thus preserved longer at some stations, but mixing was still so large that the deep water column was homogenized too much.

3.5.3 800×800 m^2 horizontal resolution

Short-term simulations (~15 days) of periods around the 2004 and 2005 CABANERA cruise were made with a model setup with 800×800 m^2 horizontal resolution. Figure 12 provides an example of how this degree of spatial resolution improves the model's ability to simulate some of the smaller-scale characteristics of the southern MIZ edge. A highly localized "jet" current of >0.3 m s^{-1} is produced near the ice edge (only U component shown in Figure 12). The horizontal density gradient caused by the vigorous melting at this location, where the ice encounters warm AW, initiates a geostrophically balanced current, directed westwards. Associated with the strong near-surface current, deep-reaching cells of alternating vertical velocity is found; producing up- and downwelling just at the ice edge. In addition to this

direct vertical advection a larger region of increased intermediate-depth (>50 m) vertical mixing is seen, larger than that both north and south of the ice edge. Large variability in time and space was seen along the ice edge during this period, in part due to intense wind systems passing by.

Due to the high computational cost of running this Barents Sea model at 800×800 m^2 resolution we were not able to run long enough simulations for comparison of seasonal development of mixing and hydrography with the results from the 4×4 km^2 resolution results presented previously.

4 Discussion

Heat fluxes and ice cover

The simulated extent of the ice cover in the Barents Sea MIZ at the time of the CABANERA cruises was found to be in fairly good agreement with satellite observations for all three survey years (section 3.1). The model thus appears able to capture the effects of interannual variations in heat fluxes and wind fields, the dominant factors influencing the ice cover. The simulations show large net heat transport with AW in the Barents Sea Opening (BSO) in 2003, a small decrease in 2004, followed by a large increase in 2005. This is in accordance with the trends for these years from measurements from a mooring array in the BSO (pers.comm. Randi Ingvaldsen, Institute of Marine Research, Bergen, Norway). Changes in the ice fluxes seem to be as important as the variability in the AW inflow through the BSO, not only for interannual fluctuations of the ice cover in the northern Barents Sea but for changes in the overall heat budget of the Barents Sea (change in heat flux with ice of 8.3 TW from 2003-2004, compared with total water heat flux change of 5.6 TW from 2004-2005).

The largest difference in ice fluxes through the straits west of Franz Josef Land was between 2003 and 2004-2005 (see Table 1). Analysis of the NCEP wind data used for the simulations shows that the annual-mean across-transect wind direction changed from negative (-1.8 m s^{-1}) in 2003 to slightly positive (0.2 m s^{-1}) in the following years. Negative wind (i.e. into the Barents Sea) would drag ice into the area. Along-transect winds may also contribute, since the drift of ice is rotated clockwise with respect to the wind direction. Negative along-transect winds would hence transport ice out of the northern Barents Sea. The NCEP data show a trend towards increased ice export also for this wind component, with annual-mean for 2003 of -1.0 m s^{-1} decreasing to -1.8 m s^{-1} thereafter. Between Franz Josef Land and Novaya Zemlya the largest ice flux change was between 2004 and 2005, with much smaller import in 2005. In this area there were no large annual-mean differences in either wind component. There was, however, a large positive wind anomaly in the winter between 2004 and 2005, with December-to-February mean of 5.2 m s^{-1} compared with smaller negative means (~ -1.0 m s^{-1}) before and after. A complete analysis of the factors influencing the ice fluxes (observed as well as modelled) can not be made without assessing i.e. sea-level trends and larger-scale atmospheric pressure differences. The trends in local winds, however, clearly agree with the changes in ice transport and we assume that these explain most of the observed variability in ice cover and transport in the northern Barents Sea during the three CABANERA survey years.

Simonsen and Haugan (1996) collected available estimates of fluxes through all the major passages connecting the Barents Sea with the surrounding areas. They report heat flux estimates ranging from 28-80 TW, with 60-80 TW being the more likely range. Net advective heat fluxes from SINMOD for the three study years are around 60-70 TW, in good agreement

with these values. A longer-term coarser-resolution model study by Maslowski et al. (2004) yielded a comparable 23-year mean net advective heat influx of ~75 TW into the Barents Sea.

Seasonal development and regional differences in vertical mixing - implications

Vertical diffusivities were found to vary greatly between winter, the melting period and the ice-free season. Spatial differences were also found, as areas of continuously enhanced mixing were identified in the northern Barents Sea. Rates of air-sea CO_2 exchange will be high in these areas. If an area covering only 10% of the whole MIZ has time-mean pycnocline diffusivity enhanced by an order of magnitude or more compared with the interior parts of the Barents Sea, a level supported by both models and measurements, this could potentially contribute with half of any net uptake of carbon from the atmosphere in this region. Also, as the ice is likely to be thinner due to large vertical heat fluxes, and more mechanically broken up due to the strong tidal currents, less wind is required for polynyas to form here than e.g. around the islands further south and west in the northern Barents Sea.

Assuming that the near-surface development of hydrography is reasonably well reproduced by SINMOD (but bearing in mind that the SML may be too deep), the coupled physical-biological model should also behave realistically with regard to physical factors influencing primary production during the main bloom that occurs when ice breaks up. The model results suggest that the pycnocline might be too strong, and diffusivities within it too low. The continued supply of nutrients through the pycnocline during the remainder of the productive season might therefore be biased low. Nutrients at the base of the pycnocline are in principle available for uptake by phytoplankton but the degree to which this takes place is regulated by the amount of light penetrating to that depth. Given typical modelled pycnocline centre depths of 25-35 m in the post-bloom/ice-free season, light limitation is likely to inhibit efficient

utilization of the deep nutrient pool. Modelled new production in the post-bloom phase is thus likely to be low, despite the large sub-pycnocline diffusivities.

In the present climate the sea ice normally disappears well after spring equinox and ample light is available for primary production to take place when the ice is gone. If the ice retreats earlier in the spring in a warmer future climate the bloom dynamics might change – incoming solar radiation would then be the limiting factor and a less intense bloom could result. Assuming that a similar amount of freshwater would be present from prior melting, the spring bloom could be more like those currently seen in fjord environments with large river runoff. Modelled pycnocline depth was shallower in the melting season than during winter (section 3.2). Maximum stratification and minimum upper-column diffusivities during peak melting typically lasted 2-3 weeks in the simulations (see Figure 6-8). During summer the SML deepens again, as wind and surface waves can intensify near-surface turbulence. Future projections of less ice and earlier melting in the Arctic thus also imply that the (modelled) post-melting increase in pycnocline depth will start earlier in the year and likely be larger by the end of the summer season. This will increase the amount of nutrients that will be accessible for primary production. Having reached the SML the dissolved nutrients will be brought further up more easily, far enough to be within the euphotic zone. The Kvitøya–Victoria area, where generally enhanced mixing rates were modelled, is likely to be a high-productivity area in a future climate with less ice.

Model – observation comparison

Differences in wind strength and the exact timing of the passing of the MIZ edge make direct comparison between model and observations difficult. Nevertheless, when comparing times of similar forcing, ice cover and stratification with the limited available observations of

vertical mixing in the Barents Sea MIZ (Sundfjord et al., 2006), the SINMOD model is capable of simulating realistic responses to wind forcing and other shear currents in the upper part of the water column (section 3.4). Modelled situations with strong wind (station XI), strong tides in shallow water (XIII), and low-energy periods (X) produced diffusivities in good agreement with measured values for the corresponding depth intervals. The modelled depths of SMLs and seasonal pycnoclines are mostly somewhat greater than those observed at the CABANERA survey stations. Observations from previous measurements campaigns in the MIZ of the northern Barents Sea were similar to those from CABANERA; Falk-Petersen et al. (2000) report melt water dilution of the upper 20 m towards the end of the melting period, either as a SML above a well-defined pycnocline at 15-20 m depth, or as a more continuous halocline from the surface and down. The overestimated pycnocline depths in the model may in part be due to the rather thick grid cells near the surface, limiting the degree to which shallow mixed layers can develop realistically. Much more observational data on turbulence would be needed to enable us to identify the specific causes of the (apparently) exaggerated SML and pycnocline depths in the model.

The modelled pycnocline is stronger than that observed – there is a too large density increase over too short a depth interval. This is intrinsically linked to diffusivity; once a too strong pycnocline has developed, the Ri-number within it will be high and mixing will remain suppressed. Measured ice drift station-mean pycnocline diffusivities (Sundfjord et al., 2006), were $>5\times10^{-4}$ m^2 s^{-1} at all stations except low-energy station X. Modelled pycnocline diffusivities averaged over the last month before all ice was gone were an order of magnitude lower at the same stations (again with the exception of X which was closer to the low observations). One would not expect long-term mean values to be identical with those of short-duration drift stations. During the field campaigns several of the drift stations had wind

speeds >10 m s^{-1}, on average producing larger diffusivity rates than the likely longer-term means for these locations. Nevertheless, it does not take many such events with mixing elevated by 1-2 orders of magnitude to influence a longer-term mean. A partial explanation for the lower modelled within-pycnocline diffusivity values is that the pycnocline is (already) too deep in the model, beyond the influence of maximum episodic wind mixing. This adds to the effect of low Ri-numbers due to exaggerated pycnocline strength.

The CABANERA turbulence measurements (Sundfjord et al., 2006) focussed on the upper part of the water column. Assessment of model performance in the near-bottom region is therefore primarily based on comparison with observed hydrography. Below the pycnocline the water column was found to be homogenized too much. Some lack of vertical structure in temperature and salinity is inherent in numerical modelling applying cell thickness of several meters but comparison with observations show also that the mean stratification is too weak. Analogous to the case of low pycnocline mixing, deep mixing can remain high once the stability has been weakened. Some enhancement of mixing is expected in the bottom boundary layer, which is typically a few tens of meters thick in this area (except near the critical latitude of the M_2 tidal component, at 74°28'N (Furevik and Foldvik, 1996; Nøst, 1994)). But the effects of bottom friction on mixing of scalars can be thought of as already being included in the vertical discretization - the deepest cell, which in our model is 50 m thick in large parts of the Barents Sea, is in fact homogenized. Friction should then not give rise to high diffusivities far away from the bottom, not further away than between the two deepest cells. Deep homogeneity could in principle be an effect of too little horizontal advection. If the characteristic AW and ArW were not supplied laterally in large enough volumes, then vertical mixing should over time erode the deep gradients. This does not seem

to be the case, as inflow currents are of similar magnitude to that observed (see also the inflow example in Figure 4).

Different vertical mixing schemes and model resolution

During winter, upper-column diffusivities in the ice-covered northern Barents Sea were larger in the MY simulations than the standard RI runs. The weak stratification at this time allowed for efficient mixing with both schemes, and this effect was largest with the MY scheme. A similar development was seen during the melting season. Modelled SML and pycnocline depth was greater in the MY simulations (on average by ~5 m), but both schemes produced too strong near-surface mixing. In shallow, strong-tide areas (e.g. station XIII) the RI diffusivity was larger and more evenly distributed in the vertical than that from MY, and closer to observations.

In a model-data inter-comparison study the performance of an earlier version of the SINMOD model was evaluated against that of a σ-coordinate model, with similar horizontal and vertical resolution, using the MY vertical mixing scheme (Hackett et al., 1995). When comparing with observational data, both models were found to reproduce the main features of the circulation system but both did also homogenize the water column too much. However, the σ-layer/MY model fared better with respect to vertical mixing than SINMOD. This was attributed primarily to MY being superior to the less sophisticated scheme applied in SINMOD. Since then SINMOD has been developed further; the vertical mixing scheme has been modified and a different horizontal diffusivity parameterization has been included (section 2.1.1), which may also affect water mass distributions. In the present CABANERA application we are not able to conclude as to which of the RI and MY turbulence schemes is better suited for our shelf MIZ simulations. Some of the differences found by Hackett et al. (1995) may also be

due to the difference in vertical layering between the two models tested there. Such differences would perhaps be larger yet between level models and isopycnal models, in which artificial diapycnal mixing is further reduced. Given the low effective mixing of the pycnocline in most areas in our MIZ simulations, however, it seems that implicit numerical mixing is not an issue of major concern in SINMOD.

Ådlandsvik and Hansen (1998) applied a 4x4 km^2 model with MY vertical mixing scheme at the Spitsbergenbanken area in the western Barents Sea. Comparing with observations of hydrography and climatology they found the modelled stratification to be too weak and the surface waters too saline in the deeper part of the area, as a result of excessive vertical mixing. However, on the shallow bank, the water column was not as homogenised as that observed, indicating too weak mixing in this part of the domain. This is similar to our findings for both RI and MY simulations; generally too strong mixing (apart from within the pycnocline proper) in the deep areas and slightly too weak in the shallow parts (see density profiles from station XIII in Figure 9). Note that the simulations of Ådlandsvik and Hansen (1998) did not include tides or ice and are therefore not directly comparable to ours.

It is not our ambition here to undertake a full comparison of all aspects of the performance of the SINMOD RI scheme with MY or other widely-used models, rather to illustrate some easily identifiable differences for our MIZ application. Clearly, the extreme variability in stratification (from nearly complete vertical homogeneity during winter to very strong stratification during peak melting), the added complexity in air-sea interaction simulation due to the presence of ice, and the need for a surface cell thickness large enough to allow for several meters of ice and surface elevation – in an area with complex topography – amounts to demanding very high versatility from the vertical mixing parameterization. A more

thorough evaluation of different options for this type of environment is certainly warranted though, both of mixing schemes and vertical discretization alternatives, in order to identify the way forward with the greatest potential for improved model performance.

Our simulations with increased vertical model resolution did show some improvements to the hydrography compared with the standard runs. However, increasing the vertical resolution alone will at best ameliorate the effects of the fundamental shortcomings of the numerical schemes and parameterizations, not resolve them. Simulations with 800×800 m^2 horizontal cell size allowed for the resolution of ice edge processes seen to increase vertical exchanges, which can potentially affect both deep-water formation and primary production at these highly dynamical locations. The along-ice edge current was up to 10 cells wide in the 800 m setup, equivalent to two 4 km cells. The standard 4×4 km^2 model runs did produce some ice edge surface currents similar to those described in section 3.5.3, but less regularly, weaker, and without the distinct accompanying upwelling and enhanced vertical diffusivity. The internal Rossby deformation radius near the MIZ edge at peak melting is ~3 km (for a 15-20 m thick SML and a density difference across the pycnocline ~1 kg m^{-3}), which can not be resolved in the standard 4×4 km^2 simulations.

The reduction of grid cell size allowed for smaller-scale advective and diffusive processes to be resolved. Increasing the resolution is thus certainly desirable, but this also implies greater computational demands. With a five-fold increase in horizontal grid cell length the number of cells is increased 25 times. In addition the time step for barotropic currents and ice elasticity must be reduced by a factor five, in total increasing CPU requirements by >100 times.

Suggestions for future experiments and model improvements

It is generally acknowledged that even the more complex turbulence schemes used in 3D ocean circulation models are imperfect, and may benefit from adaptations for application in certain ocean environments. For the MY model, for instance, it has been suggested to include a Ri-based model for the strong-shear/stable-stratification pycnocline interval (Kantha and Clayson, 1994), to improve fluxes between the mixed and intermediate depth layers. Several studies have compared different vertical mixing schemes in otherwise identical models. Most of these experiments have been for deep, open-ocean test cases. An illustrative shelf example is that of Durski et al. (2004), where the MY scheme is compared with the KPP mixing scheme (Large et al., 1994). The original KPP model employs boundary layer theory for the surface layer and then applies a gradient Ri-number-based diffusivity for the water column below the surface interval. For shallow areas Durski et al. (2004) found that this hybrid scheme produced unrealistically high intermediate and near-bottom mixing and therefore appended the model with a bottom boundary layer scheme similar to that used near the surface. This was found to produce more credible vertical distribution of diffusivity for shallow locations, and a similar modification of the SINMOD model should be tested. When comparing MY simulations with those from the modified KPP scheme Durski et al. (2004) found that the latter produced stronger near-surface mixing when the underlying pycnocline was weak. This would indicate that the KPP scheme might not be advantageous for simulations of the winter season in the MIZ, where also MY was seen to produce excessive upper-column mixing in our simulations. They did, however, find that their KPP version gave stronger mid-column mixing than MY in shallow areas. Timmermann and Beckmann (2004) compared the performance of several widely-used mixing parameterizations in the Weddell Sea (e.g. MY and KPP), both over the continental shelf and the deep sea. They found that a Ri-based scheme (Pacanowski and Philander, 1981), given a lower maximum diffusivity and augmented with an increased, constant diffusivity in a near-surface interval (determined by

the Monin-Obukhov length) to account for wind-driven mixing, was most successful at reproducing both deep winter mixing and melting period stratification in this seasonally ice-covered area. This type of modification, accounting for enhanced mixing by e.g. wind-driven ice keel drag, could be tested also for the SINMOD Ri-scheme, where the effect of breaking wind waves is suppressed during the ice covered period.

Some potentially important physical processes are not included in the commonly used turbulence schemes. Breaking internal waves can contribute significantly to mixing in ice-covered areas (Padman and Dillon, 1991) and on shelves more generally (Inall et al., 2000; MacKinnon and Gregg, 2003). The effect of internal waves on mixing may be parameterized e.g. as a function of current shear versus water column stability (for the stratified interior water column and pycnocline interval) (Gregg, 1989) or as a function of the barotropic current speed and topographic roughness parameters (for the near-bottom region) (St Laurent et al., 2002). Issues related to variable vertical cell height, in addition to the general understanding of propagation and breaking of internal waves being incomplete, makes this task non-trivial. A simple first approach is to increase the background or minimum diffusivity in areas where internal waves are likely to be of importance (Large et al., 1994). Double-diffusion may enhance vertical fluxes of heat and salt when both salinity and temperature either decrease or increase with depth. The latter type of stratification is common in our study region and double-diffusive convection has been observed in the Arctic Ocean (e.g. Rudels et al., 1999), over the northern Barents Sea shelf slope (Perkin and Lewis, 1984) and within the Barents Sea itself (Sundfjord et al., 2006). Large et al. (1994) suggested including increased diffusivity from double-diffusion as a function of the density ratio. As a minimum, there is reason to consider enhancing background diffusivity when the stratification is favourable for double-diffusion to take place.

We have shown that SINMOD can produce realistic upper-ocean responses in the MIZ, but also that adjustments are needed to get a better distribution of the mixing energy and resulting stratification. Over time, near-surface and sub-pycnocline mixing appear to be too high while diffusivity within the pycnocline may be too low in our simulations of the Barents Sea MIZ. Experiments with different turbulence initiation thresholds and other minimum and maximum values are needed to find parameter combinations that give more realistic hydrography in all domains and at all depths, if the Ri-number based scheme is to be improved. The large deep mixing could be suppressed by imposing a Law-of-the-wall function or boundary layer mixing length scaling for calculation of near-bottom diffusivity. Another possibility is to change the dependence on water column stratification to suppress the high deep mixing. The Ri-number threshold could be made dependent on stability, so that a lower Ri-number is needed for vigorous mixing to occur when stability is weak.

Future experiments with the MY scheme should, in addition to adjusting the minimum and maximum K values, include tests with increased values for one of the parameters (E_3) used in the calculation of the turbulence macro length scale (instead of imposing a limit on this length scale as is commonly done), as suggested by Burchard (2001). The local mixing length scale would then be determined prognostically for a larger part of the interior water column. In a shelf experiment Burchard (2001) showed that the mixing length (and thus diffusivity) is suppressed both in the surface mixing layer and below the pycnocline, compared with the standard MY version, during episodic strong wind forcing. Such adaptation may improve the MY performance during winter in the Barents Sea.

The enhancement of near-surface diffusivity as a function of wind-waves in the RI scheme (section 2.2.3) is suppressed if the ice thickness is >0.1 m. Waves can, however, have an effect several kilometres into the ice pack, and for optimal simulation of the near-edge processes the wave function could be made dependent also on ice cover fraction, by reducing the wave-enhancement as ice cover increases up to e.g. 50 % (even if thickness is larger than the 0.1 m threshold). The standard MY scheme does not explicitly include wave effects. Several authors have found that surface mixing is often underestimated in ocean circulation models that do not include a wave parameterization, leading to too shallow SMLs (Craig and Banner, 1994; Ezer, 2000; Mellor, 2003). Qiao et al. (2004) defined a wave-induced vertical diffusivity from the Reynolds stress expression. When adding this to the diffusivity calculated in the MY scheme they reported improved simulation of temperature distribution in the upper 100 m. This should also be tested in future SINMOD simulations with the MY scheme, possibly with an adaptation for the region close to the ice edge.

5 Summary

The seasonal patterns of stratification and vertical mixing in the Barents Sea MIZ are described through model simulations. During winter, when vertical stability is weak, diffusivities are large throughout the water column. As ice melts during spring a surface mixed layer and strong seasonal pycnocline develops. Pycnocline diffusivities are significantly lower during this period than at similar depths during winter. After all ice has disappeared the surface mixed layer deepens as buoyancy input near the surface decreases and the effect of wind penetrates deeper. Certain shallow areas with strong tidal currents in the very northern part of the Barents Sea are subject to strong vertical mixing throughout the year. Model performance is evaluated against available observations of turbulence and

hydrography. The model is able to reproduce diffusivity profiles during episodes of strong wind and tides as well as calm periods, but over time the modelled surface layer and near-bottom mixing appears to be overestimated, producing deeper surface mixed layers than observed and homogenizing the deep water column too much. Diffusivities within the pycnocline, on the other hand, are small and the pycnocline becomes steeper than that observed. Results from the Ri-number-based mixing scheme routinely used in the model are compared with those from a standard Mellor-Yamada Level 2.5 scheme. Seasonal differences in the vertical distribution of diffusivities and depths of the surface mixed layer and pycnocline are identified. We can not from these limited experiments conclude which scheme is better for our MIZ simulations, but it seems evident that both would benefit from parameter adjustment or more comprehensive amendments. Simulations with enhanced horizontal and vertical model resolution are also explored. Simulations with smaller horizontal grid cell size in particular are promising, as ice-edge processes including vertical exchanges are better resolved.

Acknowledgements

This work was supported by the Norwegian Research Council project grant 155936/S30, project 'CABANERA'. CPU quotas on the supercomputer snowstorm.uit.no were provided by NOTUR. Climatological data (NODC_WOA98) are provided by NOAA/OAR/ESRL PSD, Boulder, Colorado, USA, from their Web site at http://www.cdc.noaa.gov/.

References

Ådlandsvik, B. and Hansen, R., 1998. Numerical simulation of the circulation in the Svalbardbanken area in the Barents Sea. Continental Shelf Research, 18(2-4): 341-355.

Ådlandsvik, B. and Loeng, H., 1991. A Study of the Climatic System in the Barents Sea. Polar Research, 10(1): 45-49.

Bates, N., 2006. Air-sea CO_2 fluxes and the continental shelf pump of carbon in the Chukchi Sea adjacent to the Arctic Ocean. Journal of Geophysical Research - Oceans, 111, C10013, doi:10.1029/2005JC00308.

Berntsen, H., Kowalik, Z., Sælid, S. and Sørli, K., 1981. Efficient numerical simulation of ocean hydrodynamics by a splitting procedure. Modeling, Identification and Control, 2(4): 181-199.

Budgell, P., 2005. Numerical simulation of ice-ocean variability in the Barents Sea region: Towards dynamical downscaling. Ocean Dynamics, 55(3-4): 370-387.

Burchard, H., 2001. On the q^2l Equation by Mellor and Yamada (1982). Journal of Physical Oceanography, 31(5): 1377-1387.

Craig, P.D. and Banner, M.L., 1994. Modeling wave-enhanced turbulence in the ocean surface layer. Journal of Physical Oceanography, 24(12): 2546-2559.

Durski, S.M., Glenn, S.M. and Haidvogel, D.B., 2004. Vertical mixing schemes in the coastal ocean: Comparison of the Level 2.5 Mellor-Yamada scheme with an enhanced version of the K-profile parameterization. Journal of Geophysical Research, 109, C01015, doi:10.1029/2002JC001702,.

Egbert, G., Bennett, A. and Foreman, M., 1994. TOPEX/Poseidon tides estimated using a global inverse model. Journal of Geophysical Research, 99(C12): 24,821-24,852.

Egbert, G. and Erofeeva, L., 2002. Efficient inverse modeling of barotropic ocean tides. Journal of Atmospheric and Oceanic Technology, 19(2): 183-204.

Ellingsen, I., Slagstad, D. and Sundfjord, A., 2006. Variability of advection through the Barents Sea and its relation to carbon flux. Deep-Sea Research - II, Submitted.

Ezer, T., 2000. On the seasonal mixed layer simulated by a basin-scale ocean model and the Mellor-Yamada turbulence scheme. Journal of Geophysical Research, 105(C7): 16843-16855.

Falk-Petersen, S. et al., 2000. Physical and ecological processes in the marginal ice zone of the northern Barents Sea during the summer melt period. Journal of Marine Systems, 27(1-3): 131-159.

Fer, I. and Sundfjord, A., 2006. Observations of upper ocean boundary layer dynamics in the marginal ice zone. Journal of Geophysical Research-Oceans, in press.

Furevik, T. and Foldvik, A., 1996. Stability at M_2 critical latitude in the Barents Sea. Journal of Geophysical Research, 101(C4): 8823-8837.

Galperin, B., Kantha, L.H., Hassid, S. and Rosati, A., 1988. A quasi-equilibrium turbulent energy model for geophysical flows. Journal of Atmospheric Science, 45: 55:62.

Gawarkiewicz, G. and Plueddemann, A.J., 1995. Topographic Control of Thermohaline Frontal Structure in the Barents Sea Polar Front on the South Flank of Spitsbergen Bank. Journal of Geophysical Research-Oceans, 100(C3): 4509-4524.

Gjevik, B., Nøst, E. and Straume, T., 1994. Model simulations of the tides in the Barents Sea. Journal of Geophysical Research-Oceans, 99(C2): 3337-3350.

Gregg, M.C., 1989. Scaling Turbulent Dissipation in the Thermocline. Journal of Geophysical Research-Oceans, 94(C7): 9686-9698.

Hackett, B., Røed, L.P., Gjevik, B., Martinsen, E.A. and Eide, L.I., 1995. A Review of the Metocean Modeling Project (MOMOP) Part 2: Model Validation Study. Quantitative

Skill Assessment for Coastal Ocean Models. Eds. D. Lynch and A. M. Davies. Coastal and Estuarine Studies, 47: 307-327.

Harms, I., 1992. A numerical study of the barotropic circulation in the Barents and Kara Seas. Continental Shelf Research, 12(9): 1043-1058.

Harms, I., 1997. Water mass transformation in the Barents Sea - application of the Hamburg Shelf Ocean Model (HamSOM). ICES Journal of Marine Science, 54(3): 351 - 365.

Harms, I., Schrum, C. and Hatten, K., 2005. Numerical sensitivity studies on the variability of climate-relevant processes in the Barents Sea. Journal of Geophysical Research, 110, C06002, doi:10.1029/2004JC002559.

Hasselmann, K., et al. (16 authors), 1973. Measurements of wind wave growth and swell decay during the Joint North Sea Project (JONSWAP). Deutsche Hydrographische Zeitschrift, 80(12): 95 pp.

Hunke, E.C. and Dukowicz, J.K., 1997. An Elastic-Viscous-Plastic Model for Sea Ice Dynamics. Journal of Physical Oceanography, 27(9): 1849-1867.

Ichiye, T., 1967. Upper Ocean Boundary-Layer Flow Determined by Dye Diffusion. Physics of Fluids, 10(9): 270-277.

Inall, M.E., Rippeth, T.P. and Sherwin, T.J., 2000. Impact of nonlinear waves on the dissipation of internal tidal energy at a shelf break. Journal of Geophysical Research-Oceans, 105(C4): 8687-8705.

Jin, M., Deal, C.J., Wang, J., Tanaka, N. and Ikeda, M., 2006. Vertical mixing effects on the phytoplankton bloom in the southeastern Bering Sea midshelf. Journal of Geophysical Research - Oceans, 111: C03002, doi:10.1029/2005JC002994.

Kaleschke, L. et al., 2001. SSM/I Sea Ice Remote Sensing for Mesoscale Ocean-Atmosphere Interaction Analysis. Canadian Journal of Remote Sensing, 27(5): 526-537.

Kantha, L.H. and Clayson, C.A., 1994. An improved mixed layer model for geophysical applications. Journal of Geophysical Research, 99(C12): 25,235-25,266.

Kowalik, Z. and Proshutinsky, A.Y., 1995. Topographic enhancement of tidal motion in the western Barents Sea. Journal of Geophysical Research, 100(C2): 2613-2637.

Large, W.G., McWilliams, J.C. and Doney, S.C., 1994. Oceanic vertical mixing: A review and a model with a nonlocal boundary layer parameterization. Reviews of Geophysics, 32(4): 363-403.

Li, S. and McClimans, T.A., 1998. The effects of winds over a barotropic retrograde slope current. Continental Shelf Research, 18(5): 457-485.

Loeng, H., 1991. Features of the Physical Oceanographic Conditions of the Barents Sea. Polar Research, 10(1): 5-18.

MacKinnon, J.A. and Gregg, M.C., 2003. Shear and Baroclinic Energy Flux on the Summer New England Shelf. Journal of Physical Oceanography, 33(7): 1462-1475.

Martinsen, E. and Engedahl, H., 1987. Implementation and testing of a lateral boundary scheme as an open boundary condition in a barotropic model. Coastal Engineering, 11(5-6): 603-727.

Maslowski, W. et al., 2004. On climatological mass, heat, and salt transports through the Barents Sea and Fram Strait from a pan-Arctic coupled ice-ocean model simulation. Journal of Geophysical Research-Oceans, 109, C03032, doi:10.1029/2001JC001039.

Mellor, G.L., 2003. The Three-Dimensional Current and Surface Wave Equations. Journal of Physical Oceanography, 33(9): 1978–1989.

Mellor, G.L. and Yamada, H., 1982. Development of a turbulence closure model for geophysical fluid problems. Reviews of Geophysics and Space Physics, 20: 851-875.

Mesinger, F. and Arakawa, A., 1976. Numerical methods used in atmospheric models. GARP Publication Series, 1(17): 64 pp.

Nøst, E., 1994. Calculating tidal current profiles from vertically integrated models near the critical latitude in the Barents Sea. Journal of Geophysical Research-Oceans, 99(C4): 7885-7901.

Pacanowski, R.C. and Philander, G.H., 1981. Parameterization of vertical mixing in numerical models of tropical oceans. Journal of Physical Oceanography, 11: 1443-1451.

Padman, L. and Dillon, T.M., 1991. Turbulent Mixing Near the Yermak Plateau During the Coordinated Eastern Arctic Experiment. Journal of Geophysical Research-Oceans, 96(C3): 4769-4782.

Perkin, R.G. and Lewis, E.L., 1984. Mixing in the West Spitsbergen Current. Journal of Physical Oceanography, 14(8): 1315-1325.

Pfirman, S.L., Bauch, D. and Gammelsrød, T., 1994. The Northern Barents Sea: Water Mass Distribution and Modification. In: O.M. Johannessen, R.D. Muench and J.E. Overland (Editors), The Polar Oceans and Their Role in Shaping the Global Environment: The Nansen Centennial Volume. AGU, Washington DC, pp. 77-94.

Price, J.F., Weller, R.A. and Pinkel, R., 1986. Diurnal cycling: Observations and models of the upper ocean response to diurnal heating, cooling, and wind mixing. Journal of Geophysical Research, 91(C7): 8411-8427.

Qiao, F. et al., 2004. Wave-induced mixing in the upper ocean: Distribution and application to a global ocean circulation model. Geophysical Research Letters, 31, L11303, doi:10.1029/2004GL019824.

Rudels, B., Bjork, G., Muench, R.D. and Schauer, U., 1999. Double-diffusive layering in the Eurasian Basin of the Arctic Ocean. Journal of Marine Systems, 21: 3-27.

Rudels, B., Jones, E.P., Schauer, U. and Eriksson, P., 2004. Atlantic sources of the Arctic Ocean surface and halocline waters. Polar Research, 23(2): 181–208.

Simonsen, K. and Haugan, P.M., 1996. Heat budgets of the Arctic Mediterranean and sea surface heat flux parameterizations for the Nordic Seas. Journal of Geophysical Research-Oceans, 101(C3): 6553-6576.

Skarðhamar, J. and Svendsen, H., 2005. Circulation and shelf-ocean interaction off North Norway. Continental Shelf Research, 25(12-13): 1541-1560.

Skogseth, R., Haugan, P.M. and Haarpaintner, J., 2004. Ice and brine production in Storfjorden from four winters of satellite and in situ observations. Journal of Geophysical Research-Oceans, 109, C10008, doi:10.1029/2004JC002384.

Slagstad, D. and McClimans, T.A., 2005. Modelling the ecosystem dynamics of the Barents Sea including the marginal ice zone: I. Physical and chemical oceanography. Journal of Marine Systems, 58(1-2): 1-18.

Slagstad, D., Støle-Hansen, K. and Loeng, H., 1990. Density Driven Currents in the Barents Sea Calculated by a Numerical Model. Modeling, Identification and Control, 11(4): 181-190.

Smagorinsky, J., 1963. General circulation experiments with the primitive equations: I. The basic experiment. Monthly Weather Review, 91(3): 99-164.

St Laurent, L.C., Simmons, H.L. and Jayne, S.R., 2002. Estimating tidally driven mixing in the deep ocean. Geophysical Research Letters, 29 (23) 2106: doi:10.1029/2002GL015633.

Støle-Hansen, K. and Slagstad, D., 1991. Simulation of currents, ice melting, and vertical mixing in the Barents Sea using a 3-D baroclinic model. Polar Research, 10(1): 33-44.

Strass, V.H. and Nöthig, E.-M., 1996. Seasonal shifts in ice edge phytoplankton blooms in the Barents Sea related to the water column stability. Polar Biology, 16(6): 409-422.

Sundfjord, A., Fer, I., Kasajima, Y. and Svendsen, H., 2006. Observations of turbulent mixing and hydrography in the marginal ice zone of the Barents Sea. Journal of Geophysical Research-Oceans, accepted.

Timmermann, R. and Beckmann, A., 2004. Parameterization of vertical mixing in the Weddell Sea. Ocean Modelling, 6(1): 83-100.

Wassmann, P., 2006. Carbon flux and ecosystem feed back in the northern Barents Sea in an era of climate change: an introduction. Deep-Sea Research - II, Submitted.

Wassmann, P., Andreassen, I., Reigstad, M. and Slagstad, D., 1996. Pelagic-benthic coupling in the Nordic Seas: The role of episodic events. In: Dworschak P. C., Stachowitsch M., Ott J. (eds.) Proceedings from the 29th European Marine Biological Symposium Vienna 1994 P.S.Z.N. I: Marine Ecology, 17(1-3): 447-471.

Wassmann, P., Slagstad, D., Wexels Riser, C. and Reigstad, M., 2006. Modelling the ecosystem dynamics of the Barents Sea including the marginal ice zone: II. Carbon flux and interannual variability. Journal of Marine Systems, 59(1-2): 1-24.

Yang, H.Q. and Przekwas, A.J., 1992. A comparative study of advanced shock-capturing schemes applied to Burgers' Equation. Journal of Computational Physics, 102(1): 139-159.

Table 1. Advective heat fluxes for the three survey years. Fluxes are specified for the most important transects for fluxes in water and ice, as totals for each of the two states and as sum total. Values are given in TW. Abbreviations are for Barents Sea Opening (BSO), Franz Josef Land (FJL), Novaya Zemlya (NZ) and Svalbard (SB).

	Heat fluxes with water			**Heat fluxes with ice**			**Total Fluxes**
Year	**BSO**	**FJL-NZ**	**Sum water**	**SB-FJL**	**FJL-NZ**	**Sum Ice**	**Sum total**
2003	51.5	7.7	67.0	-5.7	-5.5	-9.8	57.2
2004	52.2	7.0	64.8	1.7	-5.6	-1.5	63.3
2005	57.5	8.5	70.4	-0.3	-2.2	-1.3	69.1

Figure 1. Map of 20 km grid model area. Depth contours at 300, 500, 1000, 2000 and 3000 m. Nested into the 20 km model is the large 4 km grid area (black rectangle) which in turn provides boundary conditions for the main 4 km/800 m model (grey rectangle).

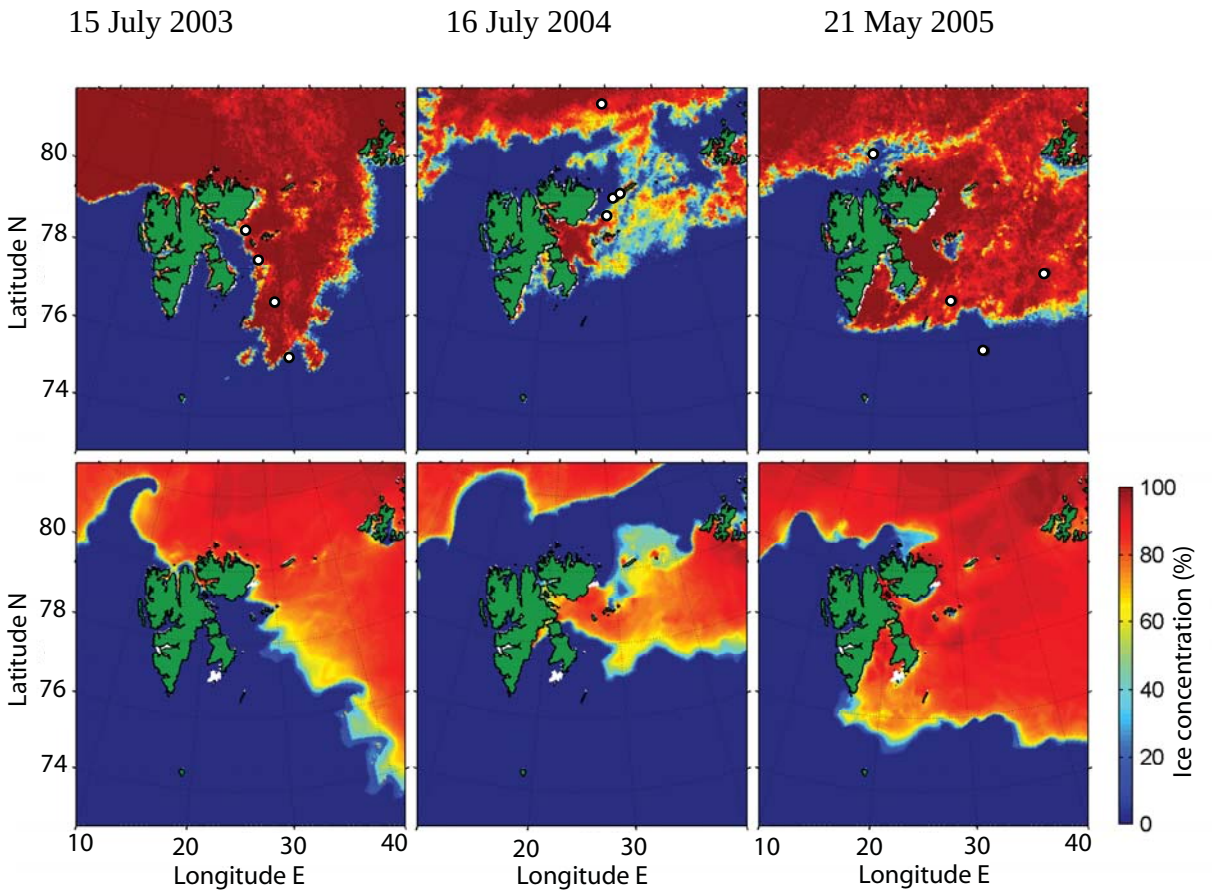

Figure 2. Ice concentration from periods of the three CABANERA surveys from satellite-derived data (upper panels, from http://iup.physik.uni-bremen.de:8084/amsr/amsre.html), and from model simulations (lower panels), for 15 July 2003 (left), 16 July 2004 (middle) and 21 May 2005 (right). Ice drift stations from the respective years are marked in the upper panels.

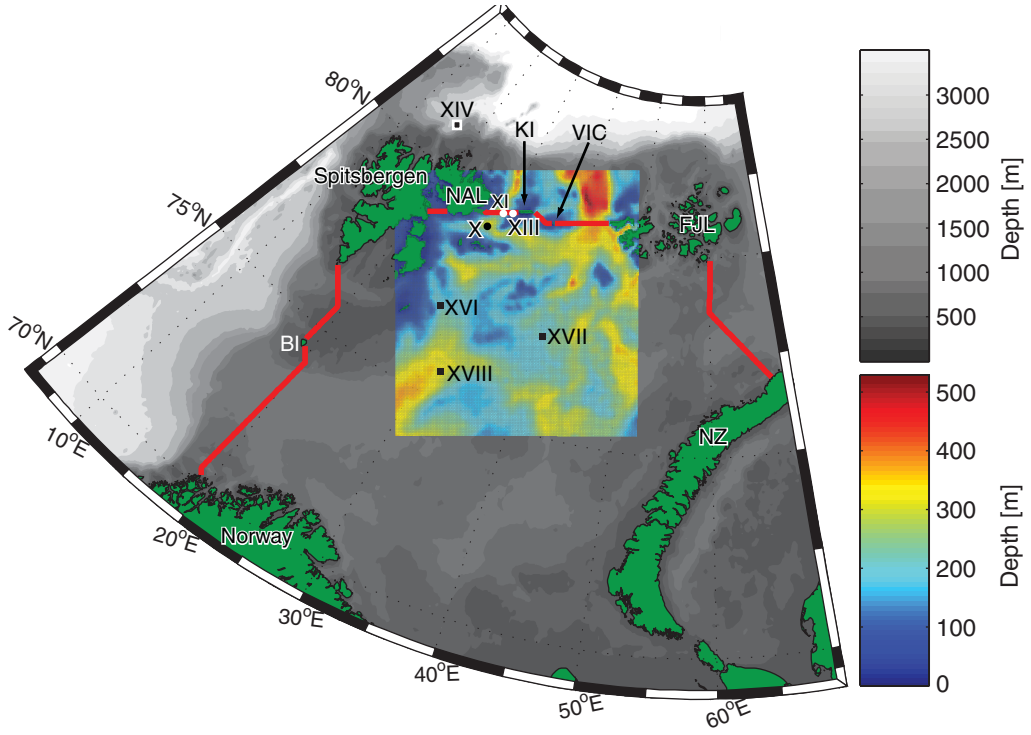

Figure 3. Bathymetric map of the Barents Sea (grey scale). The domain of the innermost model grid is shown with separate colour scale. Red lines indicate transects used in calculations of volume, heat and ice fluxes. Survey stations (roman numerals) used for time series analysis and comparison with observations are shown as dots (2004) and squares (2005). Abbreviated geographical locations are Bear Island (BI), Nordaustlandet (NAL), Kvitøya (KI), Victoria (VIC), Franz Josef Land (FJL) and Novaya Zemlya (NZ).

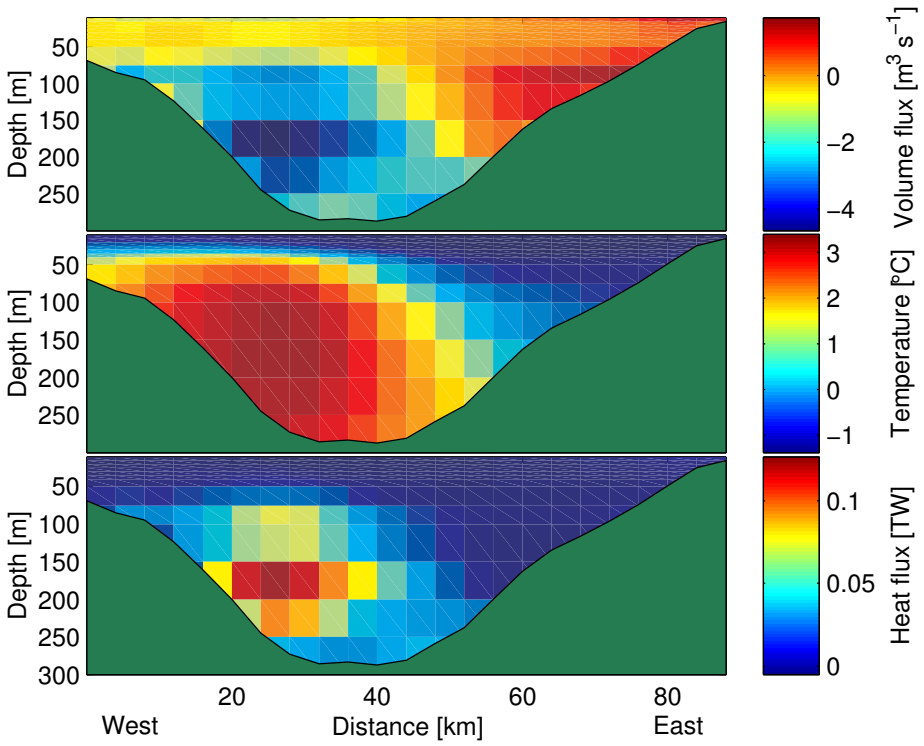

Figure 4. Cross-section from Nordaustlandet (West) to Kvitøya (East). Upper panel shows annual mean volume flux in each cell (negative flux is southward, into the Barents Sea), middle panel is mean temperature and lower panel is mean heat flux (positive fluxes contribute positively to Barents Sea heat budget). Data are from simulations of year 2005.

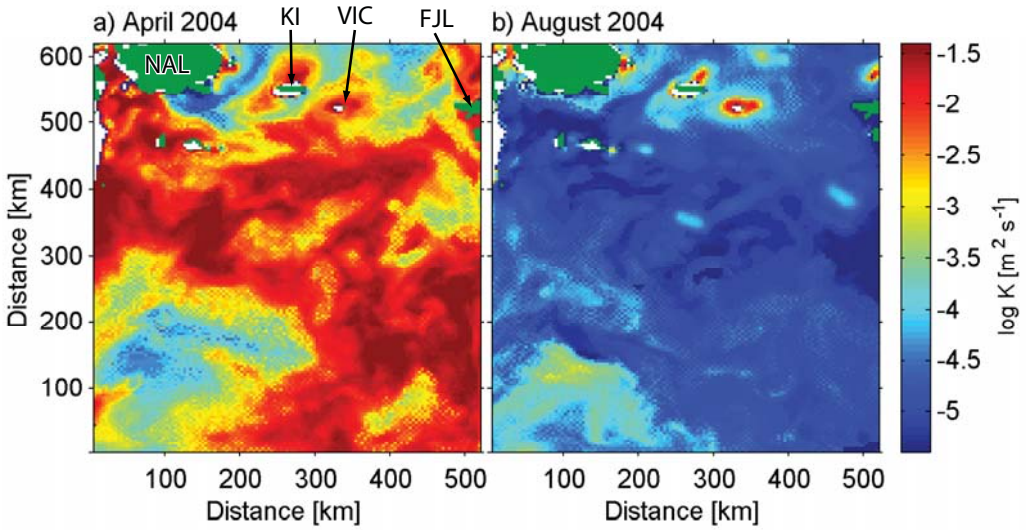

Figure 5. Simulated monthly mean of diffusivity K averaged over depth interval 25-40 m for a) April 2004 and b) August 2004 for the northern Barents Sea (note logarithmic scale for K). White areas denote depths <40 m. Indicated locations are Nordaustlandet (NAL), Kvitøya (KI), Victoria (VIC) and Franz Josef Land (FJL).

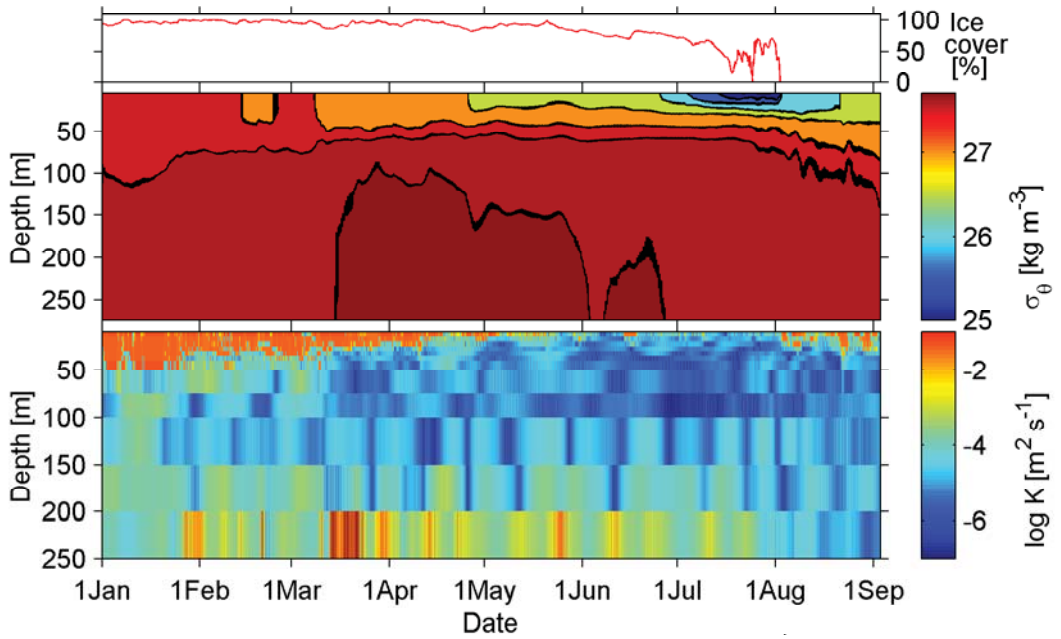

Figure 6. Simulated temporal evolution of ice cover (upper panel), density (middle panel) and diffusivity K (lower panel, note logarithmic scale) at station X, south-west of Kvitøya (2004). Model data from every 15 minutes. Bottom depth at the station is 275 m.

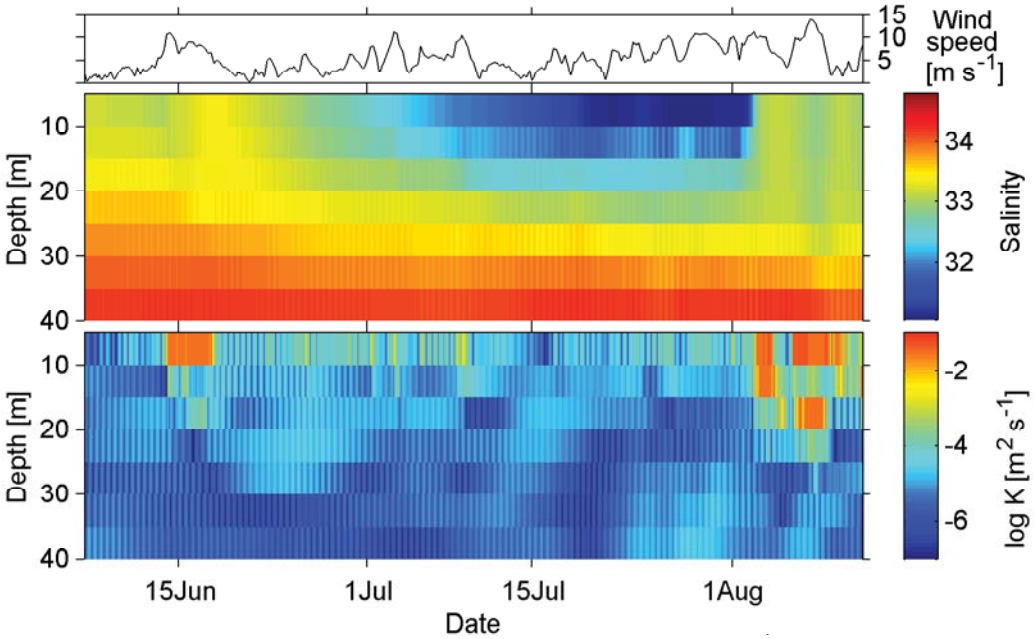

Figure 7. Wind forcing (upper panel), salinity (middle panel) and diffusivity K (lower panel, note logarithmic scale) in the upper part of the water column during the last part of the ice covered period at station X, south-west of Kvitøya (2004). Model data from every 15 minutes. Bottom depth is 275 m.

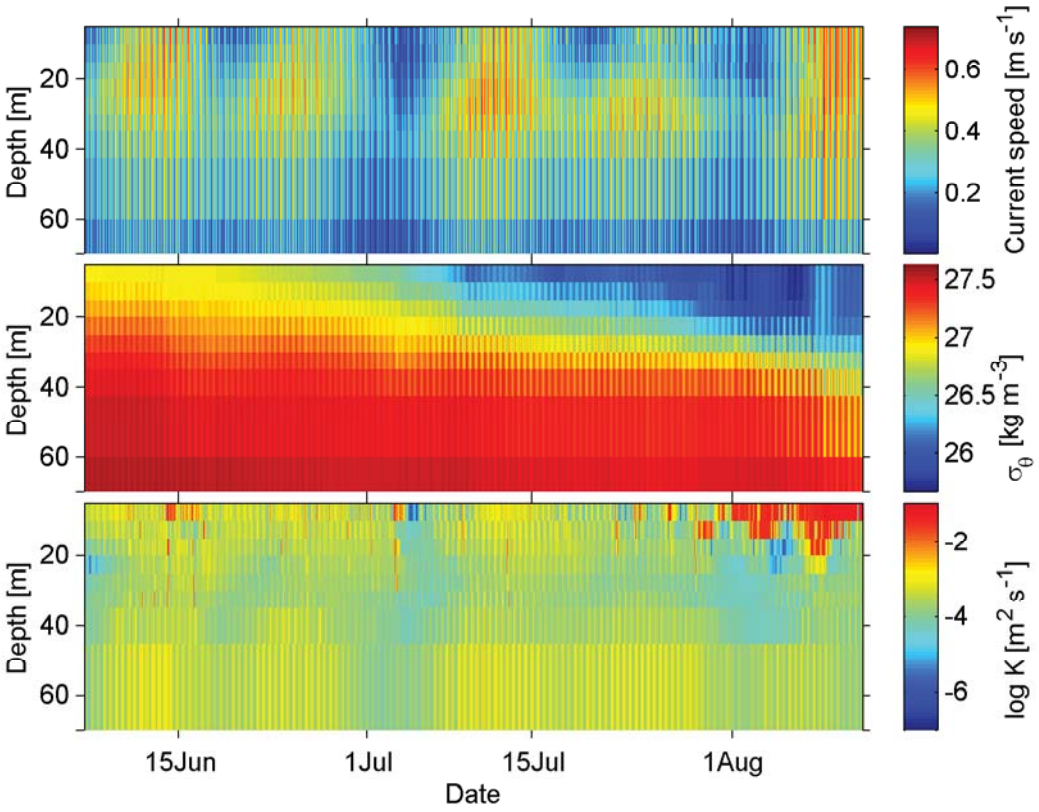

Figure 8. Current speed (upper panel), density (middle panel) and diffusivity K (lower panel, logarithmic scale) during the last part of the ice covered period at shallow station XIII, near Kvitøya (2004). Data from every 15 minutes. Bottom depth is 95 m.

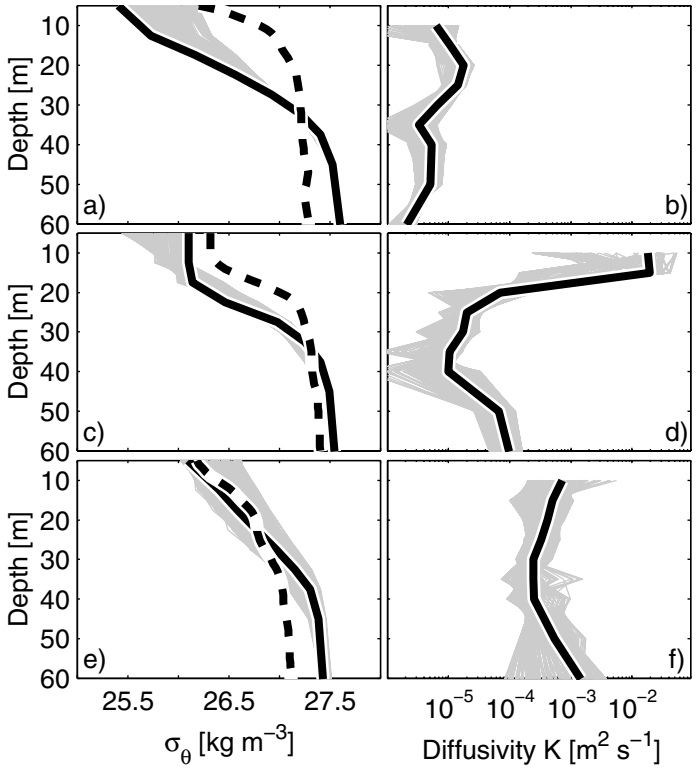

Figure 9. Vertical profiles of density (left panels) and diffusivity (right panels, logarithmic scale) at three locations in the northern Barents Sea MIZ. Grey shaded (model) density profiles are from every 15 minutes from the two-week period before the thick black model profiles. Stippled black lines are measured density profiles. Grey (model) diffusivity profiles are 48 hours of profiles yielding the thick black mean profiles. a)-b) are St X, c)-d), St XI, and e)-f), St XIII.

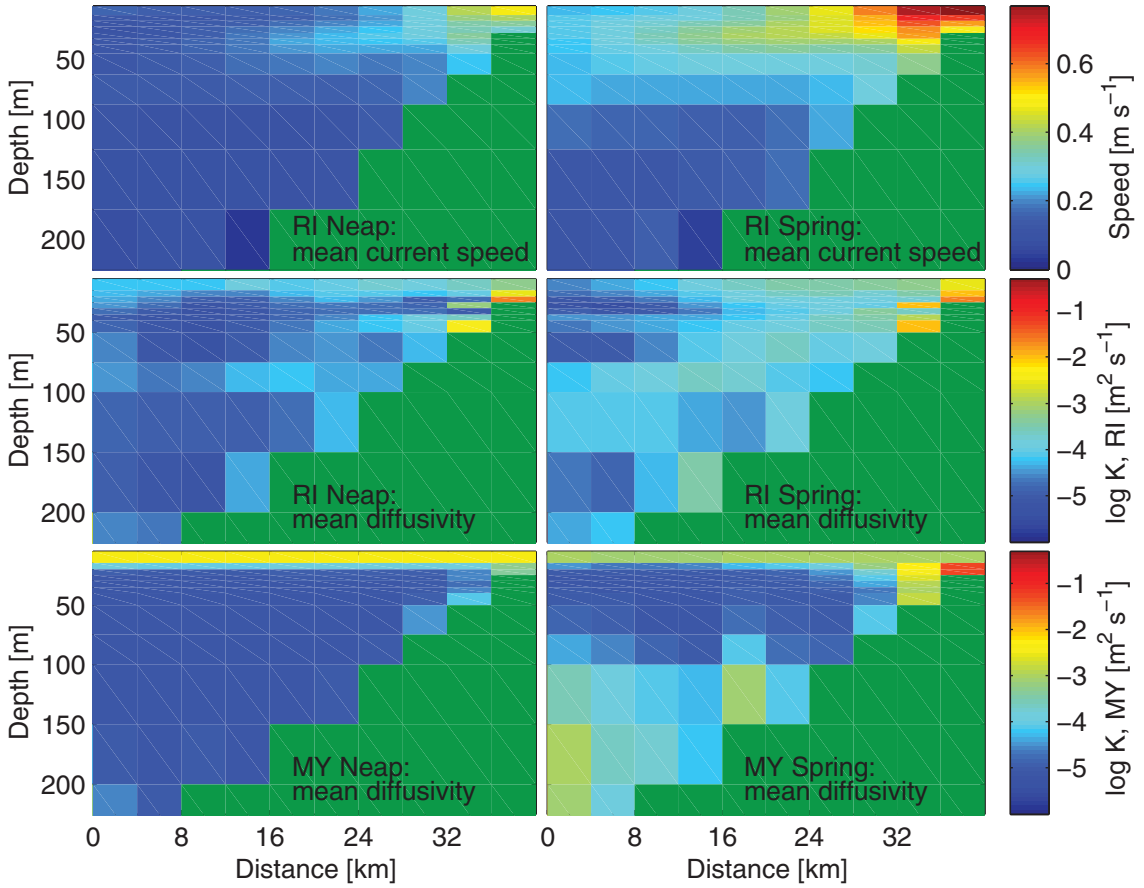

Figure 10. West to East transect across eastern half of Kvitøyrenna Trench. Upper panels show mean current speeds for neap (2-8 July 2004, left panel) and spring tide period (9-15 July, right panel) from RI simulations. Middle panels show mean diffusivities from RI mixing scheme during neap (left panel) and spring period (right panel) while the lower panels show diffusivities from MY scheme for the same periods.

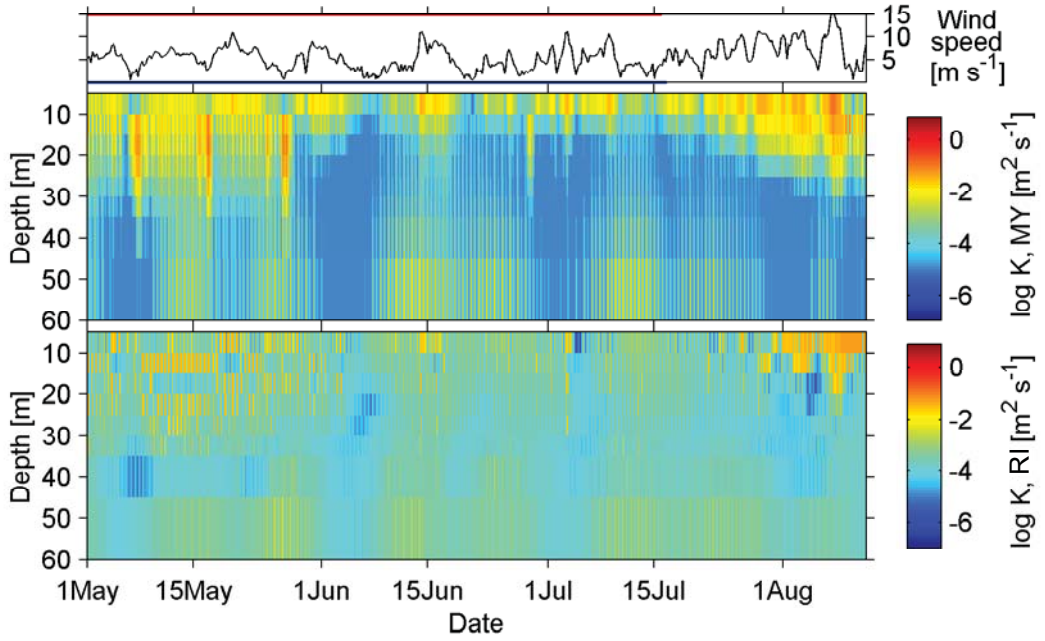

Figure 11. Comparison of diffusivities as calculated in MY (upper large panel) and RI simulations (lower panel), for station XIII. Wind speed is shown on top, and the presence of ice cover > 10% for MY (red) and RI (blue) is marked on the upper and lower borders of the wind plot.

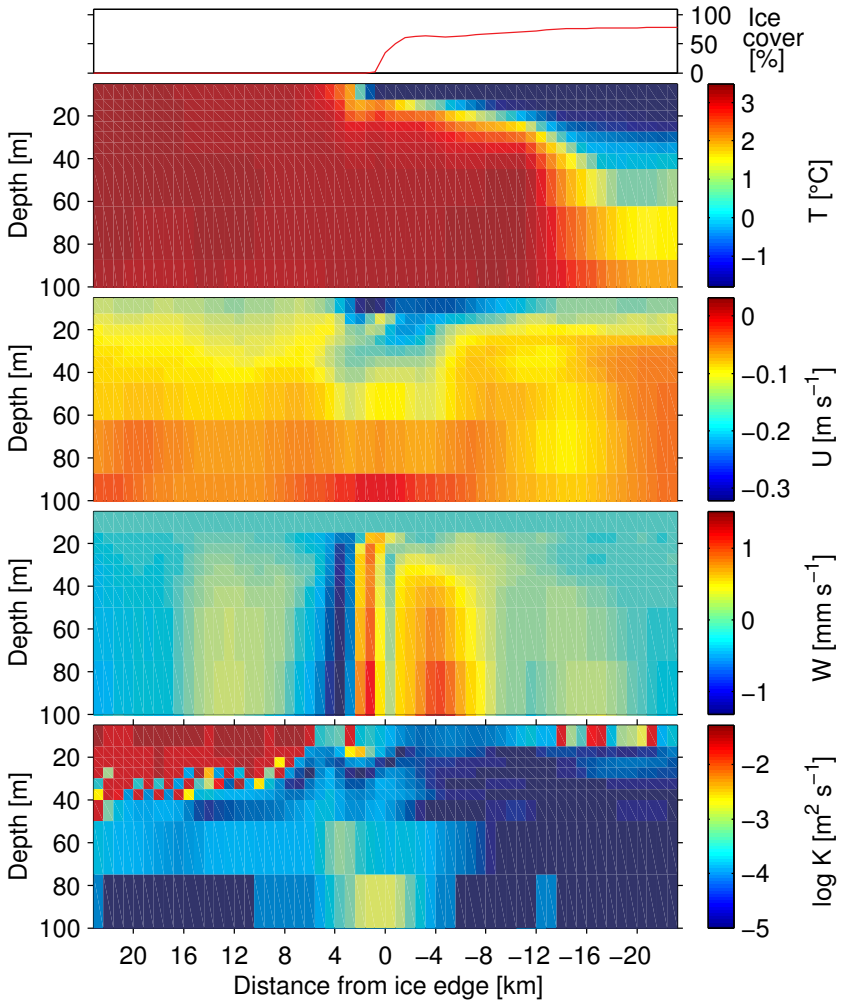

Figure 12. Transect across the ice edge in the central Barents Sea from simulations with 800×800 m^2 horizontal resolution, from south-south-east (left) to north-north-west (right), 29 May 2005. From top to bottom, panels show ice concentration, water temperature, horizontal U velocity (roughly east-west, i.e. along the ice edge), vertical velocity W (note different velocity scale from U) and log of diffusivity K.